



# Mechanism of stress distribution and failure around two different shapes of openings within fractured rock-like materials

FAN Xiang(范祥)<sup>1\*</sup>, YANG Zhi-jun(杨治军)<sup>1,2</sup>, HONG Ming(洪铭)<sup>1</sup>, YU Hao(余灏)<sup>1</sup>, XIE Yong-li(谢永利)<sup>1</sup>

1. School of Highway, Chang'an University, Xi'an 710064, China;

2. Gansu Province Transportation Planning, Survey & Design Institute Co., Ltd., Lanzhou 730030, China

© Central South University 2022

**Abstract:** The complexity of a rock masses structure can lead to high uncertainties and risk during underground engineering construction. Laboratory tests on fractured rock-like materials containing a tunnel were conducted, and two-dimensional particle flow models were established. The principal stress and principal strain distributions surrounding the four-arc-shaped and inverted U-shaped tunnels were investigated, respectively. Numerical results indicated that the dip angle combination of preexisting fractures directly affects the principal stress, principal strain distribution and the failure characteristics around the tunnel. The larger the absolute value of the preexisting fracture inclination angle, the higher the crushing degree of compression splitting near the hance and the larger the V-shaped failure zone. With a decrease in the absolute value of the preexisting fracture inclination angle, the compressive stress concentration of the sidewall with preexisting fractures gradually increases. The types of cracks initiated around the four-arc-shaped tunnel and the inverted U-shape tunnel are different. When the fractures are almost vertical, they have a significant influence on the stress of the sidewall force of the four-arc-shaped tunnel. When the fractures are almost horizontal, they have a significant influence on the stress of the sidewall of the inverted U-shaped tunnel. The findings provide a theoretical support for the local strengthening design of the tunnel supporting structure.

**Key words:** tunnel; fractured rock-like material; 2D particle flow code; crack initiation; stress distribution

**Cite this article as:** FAN Xiang, YANG Zhi-jun, HONG Ming, YU Hao, XIE Yong-li. Mechanism of stress distribution and failure around two different shapes of openings within fractured rock-like materials [J]. Journal of Central South University, 2022, 29(6): 1916–1932. DOI: <https://doi.org/10.1007/s11771-022-5048-z>.

## 1 Introduction

Jointed rock masses are widely found in nature. Owing to the uncertainty in the distribution of internal joints and fractures, the mechanical properties of rock masses are significantly discrete. Thus, research on this aspect has always been challenging in modern rock mechanics. The discreteness of rock masses increases the

complexity and risk of engineering construction. Underground engineering projects have been gradually increasing for a long time. The mechanical characteristics of jointed rock masses subject to excavation disturbances have been investigated. Numerous studies [1–4] have been conducted in this regard including theoretical mechanisms, experiments and practical applications. Early researches focused on fracture mechanics, rock mechanics, and material mechanics. The

**Foundation item:** Project(41807241) supported by the National Natural Science Foundation of China; Project(2021M693544) supported by China Postdoctoral Science Foundation; Project(2022JM-160) supported by the Natural Science Basic Research Program of Shaanxi, China

**Received date:** 2021-10-09; **Accepted date:** 2022-03-08

**Corresponding author:** FAN Xiang, PhD, Associate Professor; Tel: +86-17791794601; E-mail: [fanxiang224@126.com](mailto:fanxiang224@126.com); ORCID: <https://orcid.org/0000-0001-7059-3954>

growth criterion and evolution law of micro-fractures around a single fracture have been explored [5 – 6]. However, actual rock masses generally have more than one fracture. Based on the research on types and cracking mechanisms of single fracture, specimens with specific fractures have been prepared via cutting or prefabrication. The initiation, growth and evolution processes of cracks models with single preexisting fracture or multiple preexisting fractures have been studied [7 – 10]. With advances in research theory and technology, further studies have not only been conducted on the single mechanical properties of jointed rock masses. Research models considering actual rock masses properties have gradually been developed. Thus, considering actual layered rock masses, specimens with horizontal fractures have been prefabricated. By changing parameters such as the number, strike, spacing, dip angle, and connectivity rate of preexisting fractures [11 – 17], using the control variable method, the influence of various factors on the overall failure mode of rock mass models has been analyzed. Furthermore, several scholars have considered the influence of fractures filling on crack evolution [18–19]. Early research on jointed rock masses approaches based on a single fracture has progressed to the study of actual rock masses properties.

Recently, for rock materials or rock-like materials under various combinations of fractures and openings, many scholars have investigated the difference in the strength and the mechanism of crack initiation, growth, and evolution of the materials. Research has been conducted from single fracture to multiple fractures as well as single round hole to multi-type porous mediums. Currently, significant research is being conducted on the cracking mechanism of rock masses models with a single-layer horizontal fracture and a cross fracture. The stress and strain characteristics of the opening hole model under the interaction of multiple fractures have been analyzed. First, for a rock-like material model with holes, by controlling the factors such as the dip angle, location, and connectivity of fractures, the influence of fractures on the failure characteristics around openings has been studied. The types of holes that have been considered include round [20–25], square [26], horseshoe [27–

28], and oval [29]. In addition, the failure characteristics of a porous rock mass model have been studied in detail. The effect of the number of holes [30], distance between holes [31], hole fillers [32], and a combination of holes and preexisting fractures inclination angle [4, 32–37] on the uniaxial compressive strength and crack evolution mode of specimens has been studied. And their corresponding influence on the mechanics, deformation, and failure characteristics of a fracture model with holes has been analyzed. On this basis, the cracking failure mechanism of fractured rock masses with holes under multiaxial stresses has been further analyzed [38].

Till now, numerous experimental and numerical modeling studies were conducted focusing on the mechanical properties, failure modes of rock masses, and their relationship with the type of rock material [39–40]. However, owing to the uniqueness of underground engineering construction and the anisotropy, complexity, and discreteness of rock masses, several other problems need to be further explored, for instance, the relation between stress or strain distribution and combination of fracture angle, and the relation between surrounding rock failure and fracture distribution. Therefore, to study the mechanical and failure characteristics of fractured rock masses more comprehensively, two types of reduction size tunnel sections were generated within fractured rock-like material models. Based on the observed failure phenomenon and combining the particle flow code approach, the failure characteristics, the principal stress and principal strain distributions around the two types of tunnel profiles within four different combinations of fracture inclination angles were analyzed. Compared with the previous researchers, the principal stress distributions and failure characteristics of tunnel sidewall under different fractures distribution forms were obtained, which provides certain theoretical support for the strengthening design of tunnel engineering supporting structure.

## 2 Experiment and numerical modeling

### 2.1 Specimen preparation

In the experiment, high-strength gypsum was also used. The water-gypsum ratio (mass ratio of

water to gypsum powder) of the rock-like materials was 1:1. Considering the fracture distribution within the actual layered rock masses, a specific simplified group of parallel fracture combinations was selected. As shown in Figure 1, the center point of the entire distribution of a single set of fractures was considered the reference point  $O$ . The angle between the fracture and the positive direction of the horizontal axis ( $x$  axis) is called the fracture inclination angle. The  $\alpha_1$  group of fractures was formed by counterclockwise rotation of point  $O$  rotation. And the  $\alpha_2$  group of fractures was formed by clockwise rotation of point  $O$  rotation. The fracture combination types required for the study were established by superposing the two fracture groups. The fracture combinations ( $\alpha_1, \alpha_2$ ) were  $(30^\circ, 30^\circ)$ ,  $(45^\circ, 45^\circ)$ ,  $(60^\circ, 60^\circ)$ , and  $(90^\circ, 180^\circ)$ . The width of the fractures was 2 mm and the maximum length of the fractures was 30 mm. The connectivity of the fractures was 0.5, the lateral spacing of the preexisting fractures was 50 mm, and the center spacing of the adjacent parallel fractures was 45 mm. A fractured specimen with a tunnel was thus established (Figure 2). Further, the dimensions were length  $\times$  width  $\times$  height = 300 mm $\times$ 300 mm $\times$ 50 mm. And the tunnel center coincided with the model center. In this study, a four-arc-shaped tunnel section and an inverted U-shaped tunnel section were selected as the research objects and scaled according to the similarity ratio. The specific dimensions are shown in detail in Figure 3. The width of the four-arc-shaped tunnel was 60 mm and the height was 48 mm. The width of the inverted U-shape tunnel was 60 mm and the height was 60 mm. In the process of specimen preparation, two types of solid columns like the designed tunnels

described above were first prepared using a 3D printing technology, and then fixed at the specimen center during the casting. Further, the fractures were generated by inserting mica sheets according to the above-mentioned configuration.

After determining the sizes of the specimen and the geometrical parameters of the fractures and joints, cube specimens were prepared using the pouring method. The parameters of the specimens including the type of tunnel and the combination of fracture inclination angles are listed in Table 1.

Thus, the specimens were numbered based on the tunnel types and combination of fractures. For example, R-30-30 indicated that the tunnel type considered was a four-arc-shaped tunnel, and the combination of fracture inclination angles considered was  $(30^\circ, 30^\circ)$ . U-30-30 indicated that the tunnel type considered was an inverted U-shaped tunnel, and the combination of fracture inclination angles considered was  $(30^\circ, 30^\circ)$ . Simultaneously, cylindrical gypsum specimens of the same age were prepared to conveniently determine the macroscopic mechanical parameters of rock-like materials. The loading test is referred to Ref. [39].

## 2.2 Creation of numerical fractured tunnel model

The calibration of meso-parameters is referred to Ref. [39]. This research model included four fracture inclination angle combinations ( $30^\circ$ - $30^\circ$ ,  $45^\circ$ - $45^\circ$ ,  $60^\circ$ - $60^\circ$ , and  $90^\circ$ - $180^\circ$ ) and two opening types (four-arc-shaped opening and inverted-U-shaped opening). The thickness of the model was one-sixth of the length and width, and the fractures and tunnels ran along the thickness direction. Thus, the three-dimensional research model was simplified to

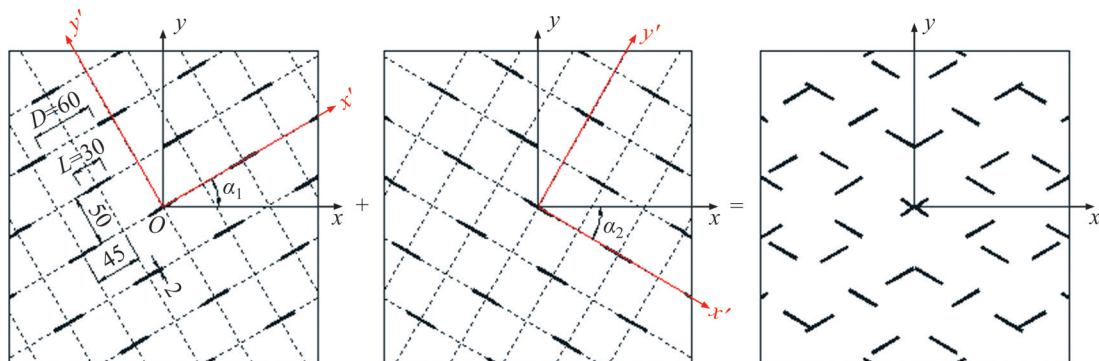


**Figure 1** Schematics of the joint geometry configurations in the specimens (unit: mm) [39]

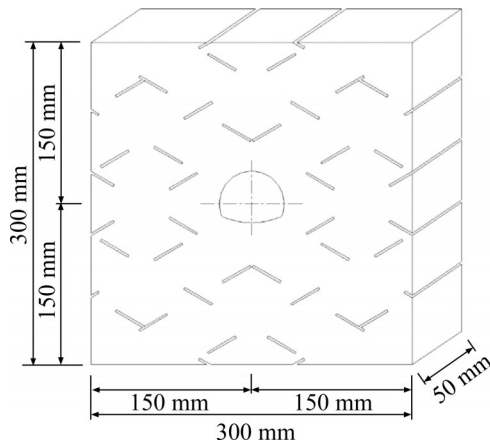


**Figure 2** Schematic of the dimensions of the specimens [39]

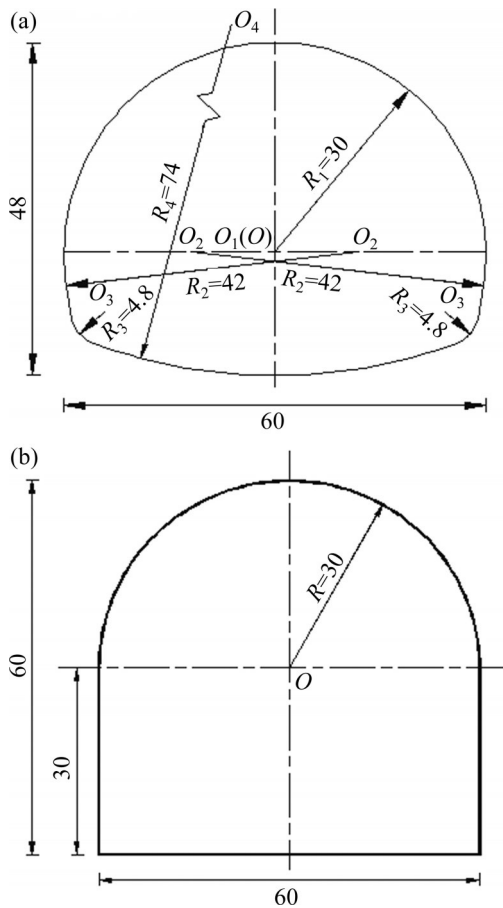


**Figure 3** Specific dimensions of four-arc-shaped tunnel section (a) and U-shaped tunnel section (b) (unit: mm)

a two-dimensional state. Subsequently, a two-dimensional particle flow model with sizes of 300 mm × 300 mm (length × width) was established. The preexisting fractures and tunnels were created using the deletion method, as shown in Figure 4. According to the eight groups of fractured tunnel models, the numerical results were obtained.

**Table 1** Tunnel type and combination of flaw angles

Number	Specimen ID	Type of tunnels	Flaw angle/(°)	
			$\alpha_1$	$\alpha_2$
1	R-30-30	R	30	30
2	R-45-45	R	45	45
3	R-60-60	R	60	60
4	R-90-180	R	90	180
5	U-30-30	U	30	30
6	U-45-45	U	45	45
7	U-60-60	U	60	60
8	U-90-180	U	90	180

Note: R and U represent four-arc-shaped and U-shaped tunnel section, respectively, and 30-30 indicates the combination of fracture inclination angle degrees of 30° and 30°.

### 3 Characteristics of crack evolution around openings

To analyze the evolution characteristics of fractures at different positions around the tunnel, a certain area around the opening was partitioned as M-1 (roof), M-2 (left spandrel), M-3 (right spandrel), M-4 (left haunch), M-5 (right haunch), M-6 (left arch), M-7 (right arch), and M-8 (floor) (see Figure 5). By comparing the results of the laboratory tests with those numerically obtained by a two-dimensional particle flow model, the macroscopic fracture characteristics of the model and the evolution characteristics of the fractures around the tunnel were obtained (see Table 2). When the tunnel section type is a four-arc-shaped tunnel, it was found that the pre-existing fracture inclination angle directly determined the cracking degree of the fractured rock masses. Furthermore, a difference in the cracking characteristics was observed around the tunnel.

The laboratory test results indicated that all specimens were prone to tensile failure at the vault or arch bottom and crushing failure near the haunch. This can lead to a V-shaped failure zone on the tunnel sidewall. For specimen R-30-30, tensile failure occurred at the arch bottom, and crushing failure occurred at the haunch. For specimen R-45-45, tensile failure occurred at the vault and arch bottom, and crushing failure occurred at the haunch. For specimen R-60-60, tensile failure occurred at the vault and arch bottom, and crushing failure occurred at the haunch. For specimen R-90-180, tensile failure occurred at the vault and

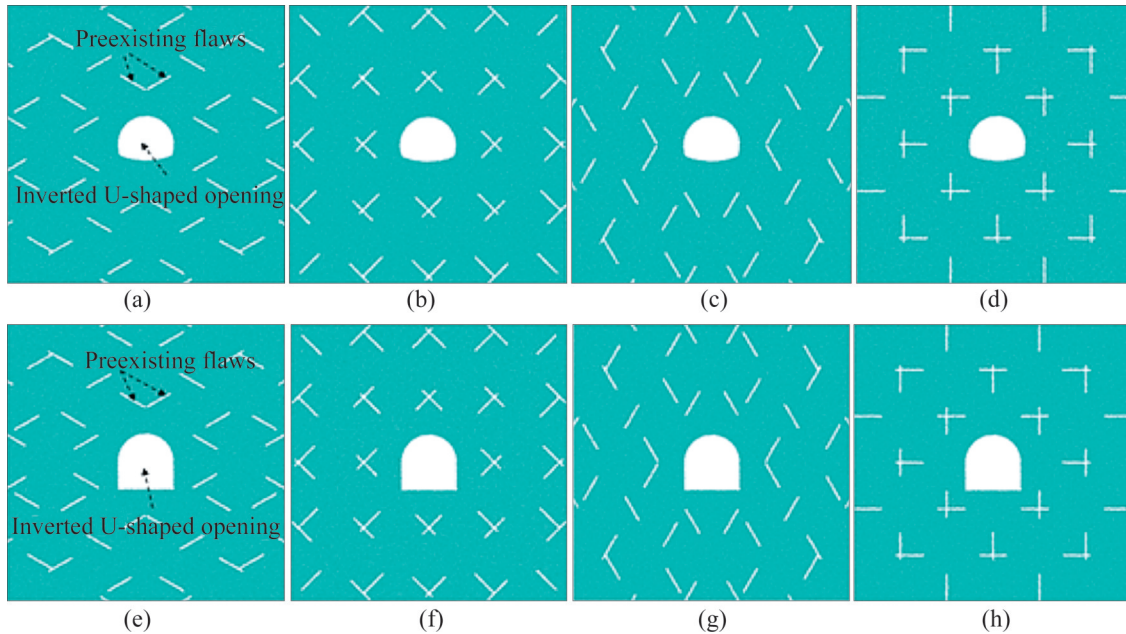


**Figure 4** Establishment of numerical fractured rock-like tunnel models: (a) R-30-30; (b) R-45-45; (c) R-60-60; (d) R-90-180; (e) U-30-30; (f) U-45-45; (g) U-60-60; (h) U-90-180

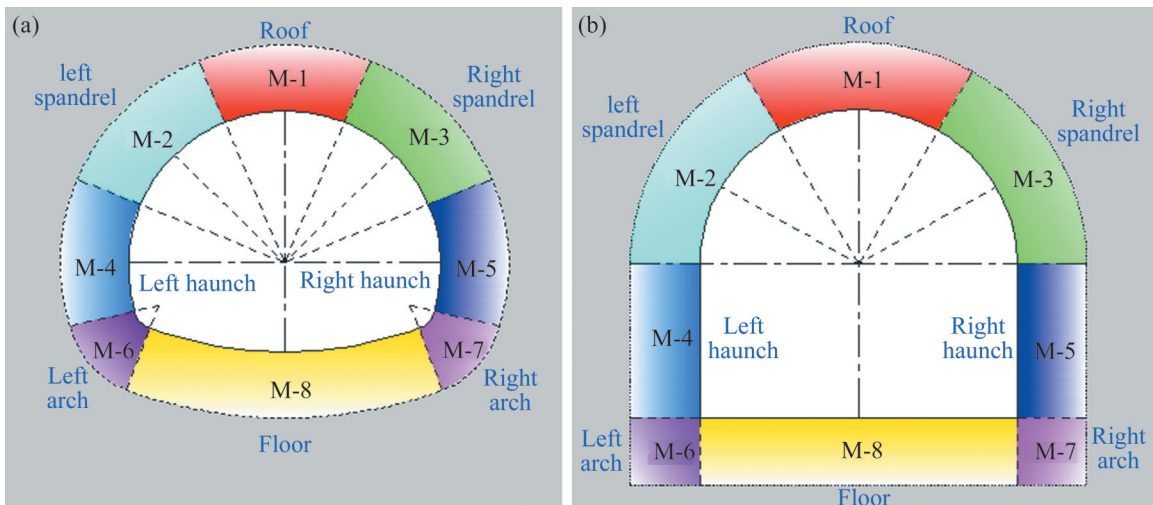


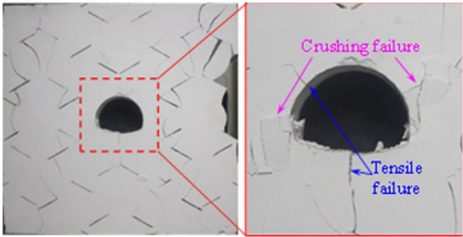
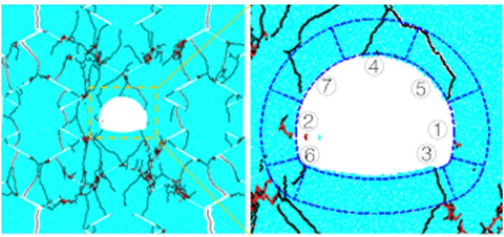
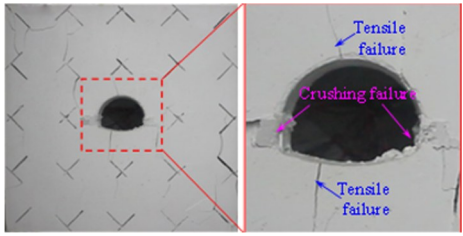
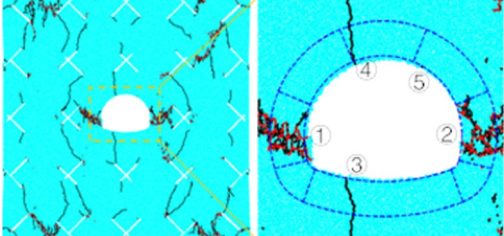
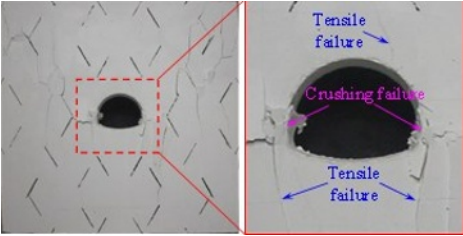
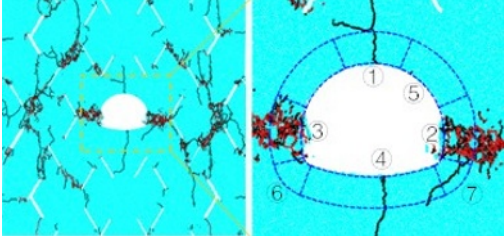
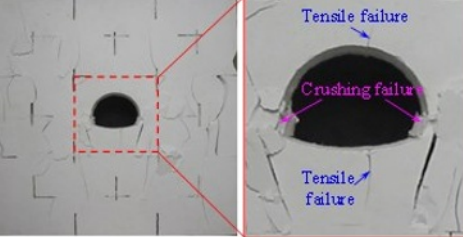
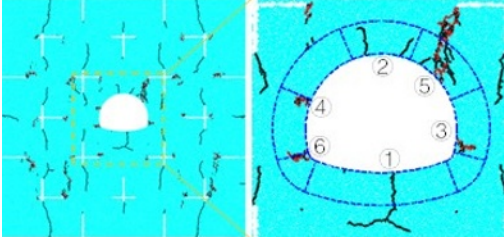
**Figure 5** Schematic diagram of the zoning around the opening: (a) Four-arc-shaped tunnel; (b) U-shaped tunnel

arch bottom, and crushing failure occurred at the hance. With an increase in the absolute value of the inclination angle of the preexisting fractures, the tunnel sidewall cracked significantly.

Combined with the numerical modeling results, different fracture inclination angles not only led to different overall crack initiation mechanisms of the fractured rock tunnel model, but also created different initiation sequences of cracks around the tunnel. Thus, by studying the zones around the tunnel, the initiation sequences of cracks around the tunnel were marked. For specimen R-30-30, micro-fractures first appeared in M-5, and then occurred in

M-4 and M-1. Finally, under uniaxial compression, micro-fractures gradually evolved into macro-cracks and spread to other modules. For specimen R-45-45, cracks were initiated around the opening mainly in M-4 and M-5, and they developed in M-1 slightly later than M-8. For specimen R-60-60, cracks around the opening mainly also appeared in M-4 and M-5, but micro-fractures appeared at the earliest in M-1. For specimen R-90-180, tensile micro-fractures appeared in M-8, but the degree of crushing failure was small near M-4 and M-5. Further, there was obvious breakage near M-2 and M-3.

**Table 2** Fracture around the four-arc-shaped tunnel (the black line is tensile micro-cracks and the red line is shear micro-cracks)

Sample ID	Experimental	Numerical
R-30-30		
R-45-45		
R-60-60		
R-90-180		

In conclusion, under the action of unidirectional stress, with an increase in the absolute value of the fracture inclination angle, the crack initiation position around the four-arc-shaped tunnel gradually transitions from the hance (M-4, M-5) to the vault (M-1). Concurrently, a positive correlation is observed between the absolute value of the fracture inclination angle and the degree of damage to the sidewall.

In the overall failure mode and the fracture around the opening, many similarities and differences were observed between the inverted U-shaped tunnel and the four-arc-shaped tunnel. When the preexisting fracture combination types were 30°-30°, 45°-45°, and 60°-60°, the overall failure modes of the two tunnel models were similar based on the experimental and numerical results (see

Table 3). However, under the preexisting fracture combination type 90°-180°, R-shaped specimens showed shear sliding failure at the spandrel (M-2 and M-3), while U-shaped specimens showed shear dislocation at the arch springing (M-6 and M-7). Combined with the failure modes determined through the numerical model, the evolution degree of cracks around the inverted U-shaped tunnel was less than that around the four-arc-shaped tunnel. However, with an increase in the absolute value of the preexisting fracture inclination angle, splitting failure near the sidewall was gradually observed to intensify, forming a V-shaped failure zone with an inward opening. Tensile cracks further developed near the failure zone (near the opening), while shear cracks were more common at the far end of the failure zone. When the combination type of the

**Table 3** Cracking around the inverted U-shaped tunnel

Sample ID	Experimental	Numerical
U-30-30		
U-45-45		
U-60-60		
U-90-180		

preexisting fracture inclination angle was  $30^\circ$ - $30^\circ$ , cracks were initiated in M-4. When the combination type of the preexisting fracture inclination angle was  $45^\circ$ - $45^\circ$ , cracks were initiated in M-6. When the combination type of the preexisting fracture inclination angle was  $60^\circ$ - $60^\circ$ , cracks were initiated in M-7.

In conclusion, when preexisting fractures are almost vertical, the stress concentration regions around the tunnel gradually shift from the vicinity of the sidewall to the top and bottom of the tunnel. Thus, the cracking order is as follows: hance→arch springing/spandrel→arch bottom/vault. For both types of tunnels, there is a consistent correlation between the fracture degree and fracture inclination angle.

## 4 Local stress and strain around tunnel

### 4.1 Qualitative analysis of stress around tunnel

To study the stress distribution characteristics around the opening, two stages were selected for the analysis: the stage of crack initiation (S-W-CI) for the whole model and the stage of crack initiation first appearing around the tunnel (S-T-CI). Thus, using the contact force monitoring function in PFC<sup>2D</sup>, the force chain distribution characteristics of each model could be obtained. The blue lines indicate compressive stress while the green lines indicate tensile stress. In addition, the thickness of the lines indicates the magnitude of the particle contact force.

As listed in Table 4, when the fractured rock tunnel model was at the stage of S-W-CI, no micro-

**Table 4** Contact force distribution around four-arc-shaped tunnel

Failure stage	R-30-30	R-45-45	R-60-60	R-90-180
S-W-CI				
S-T-CI				

fractures appeared. With a decrease in the absolute value of the preexisting fracture inclination angle ( $60^\circ \rightarrow 45^\circ \rightarrow 30^\circ$ ), the compressive stress concentration of the sidewall with the preexisting fractures gradually increased. Simultaneously, the tensile stress concentration near the vault and arch bottom reduced (the green areas became lighter), and the compressive stress concentration near the hance also reduced (the blue areas became lighter). This indicates that the distribution of the inclination angle of the preexisting fractures directly determines the transmission effect of the axial load.

As shown in Figure 6, the influence of preexisting fractures on the stress around the tunnel was plotted, and a law of axial stress transfer was established. When preexisting fractures are arranged almost horizontally, under the action of an external load, during the downward transmission of the axial stress ( $\sigma_N$ ), a triangular tensile stress zone appears around the lateral wall of preexisting fractures in the horizontal direction, which causes the axial stress to decrease ( $k_1 > 1$ ).  $1/k_1$  and  $1/k_2$  are the assumed reduction coefficients. The reduced axial stress ( $\sigma_N'$ ) causes the tensile stress areas at the vault and arch bottom of the tunnel and the compressive stress areas at the arch waist to decrease. However, when preexisting fractures distributed vertically, the triangular tensile stress areas around the sidewall of preexisting fractures in the vertical direction are much smaller than those of horizontal fractures, which reduces the axial stress loss ( $k_1 > k_2 > 1$ ). Thus, the concentration of the compressive stress and tensile stress around the tunnel increases. In addition, because of the absence of a filler in the middle of the fractures, a “squeezing and closing”

tendency under the action of axial stress is observed, which further affects the cracking degree around the tunnel.

At the beginning of S-T-CI, mixed microfractures appeared in the tunnel sidewall of specimens with the preexisting fracture combination type 30-30. Tensile cracks and shear microfractures appeared near the preexisting fractures. Simultaneously, when compared with models of different fracture combination types, crack initiation was observed in several positions around the tunnel with an increase in the absolute value of the fracture inclination angle. However, the degree of cracking around preexisting fractures was reduced until no cracking occurs. Tensile microfractures (cracks) mainly developed owing to the preexisting vertical fractures. Small tensile stress existed near the new cracks (the green areas became lighter), but large tensile stress existed at the crack tip (the green areas became darker). Thus, the cracks had a tendency to continuously expand. Contrarily, the shear microfractures were mainly distributed in areas with a high compressive stress concentration and almost no tensile stress.

The influence of preexisting fracture distribution characteristics on the stress around the tunnel for the inverted U-shaped tunnel model was consistent with that of the four-arc-shaped tunnel model (see Table 5).

The failure of the model was observed to be from S-W-CI to S-T-CI. Owing to the increase in the overall fracture degree of the model, the tensile stress areas near the vault and arch bottom gradually decreased, but the compressive stress areas gradually increased. Simultaneously, the



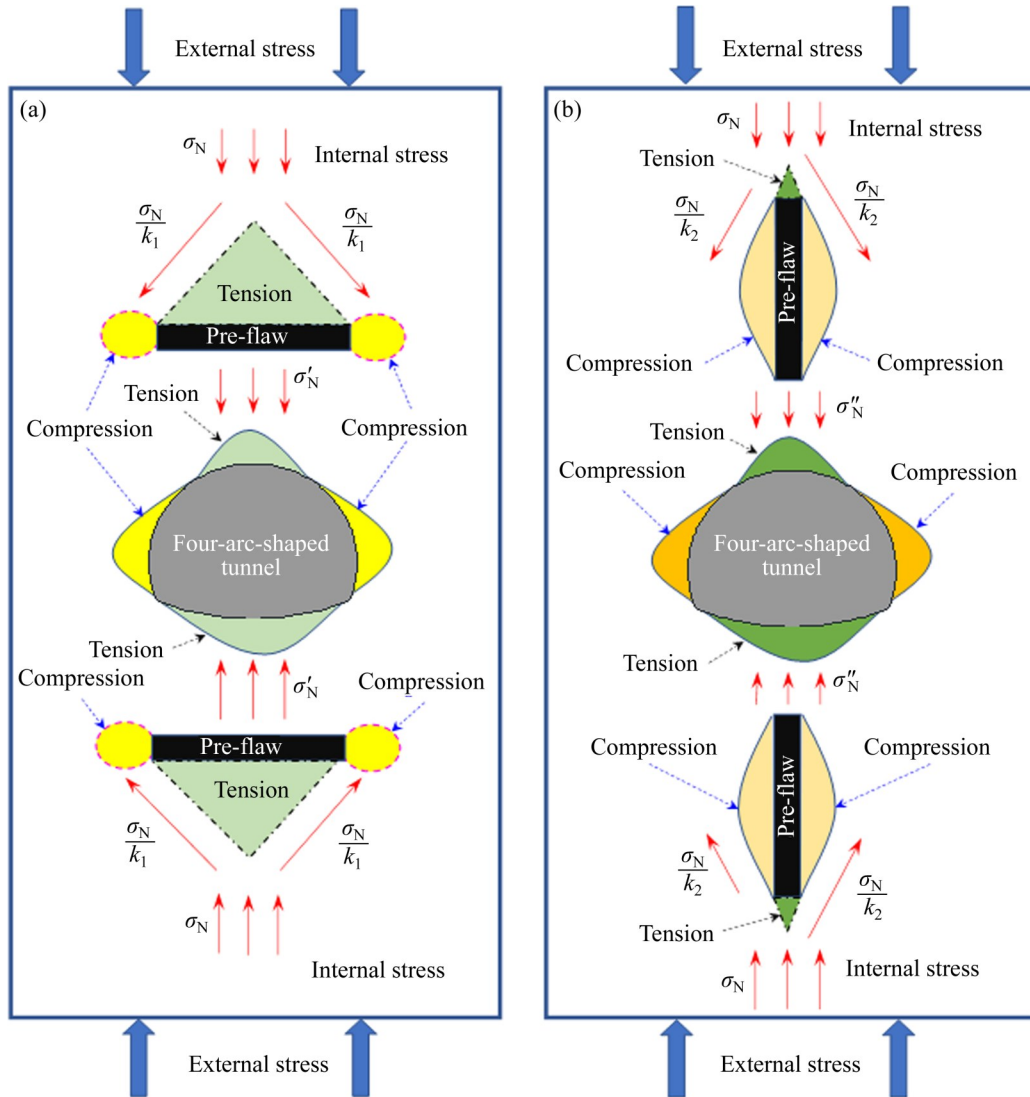


**Figure 6** Effect of flaw on stress around four-arc-shaped tunnel: (a) Horizontal flaws; (b) Vertical flaws

**Table 5** Contact force distribution around inverted U-shaped tunnel

Failure stage	U-30-30	U-45-45	U-60-60	U-90-180
S-W-CI				
S-T-CI				

compression stress concentration near the hance (sidewall) of the tunnel became increasingly evident. In the specimens with fracture inclination

angle combinations of 30°-30°, the aforementioned laws were more obvious. This shows that the fracture inclination angle combination not only has

an impact on the stress concentration degree around the tunnel, but also has a relatively large impact on the stress attenuation amplitude during crack evolution.

### 4.2 Quantitative analysis of stress around tunnel

To compare and analyze the stress and deformation characteristics around the two tunnels, as illustrated in Figure 7, the measured circles were arranged at the vault (I), left spandrel (II), right spandrel (III), left hance (IV), right hance (V), left arch springing (VI), right arch springing (VII), and arch bottom (VIII) to monitor the stress and strain at each position. The prescribed positive direction of the principal stress and principal strain is consistent with that in rock mechanics theory.

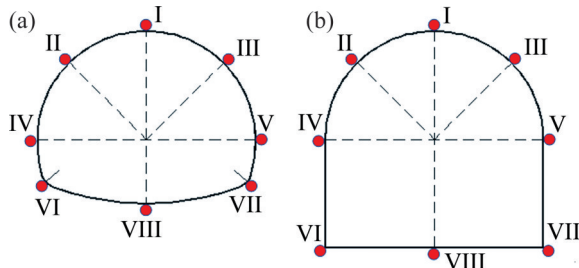


**Figure 7** Measure point layout: (a) Four-arc-shaped tunnel; (b) U-shaped tunnel

As shown in Figures 8 and 9, when the axial stress of each model reached 0.5 MPa, the stress distribution characteristics around different tunnel types were affected by different fracture combination types. When a four-arc-shaped tunnel type was considered, the absolute value of the minimum principal stress reached a maximum at the vault and arch bottom. The minimum principal stress at the other positions was approximately zero. Hence, under uniaxial stress, the vault and arch bottom are under tensile stress, and the sidewall is almost free from tensile stress. Simultaneously, the maximum principal stress is approximately zero at the vault and arch bottom. And the maximum principal stress is positive at the other positions. The tunnel sidewall (i. e., the other position) is mainly under pressure, and the vault and arch bottom are not under pressure. The distribution characteristics of the principal stress around the inverted U-shaped tunnel are consistent with those of the four-arc-shaped tunnel.

Under the same axial stress level, the tensile

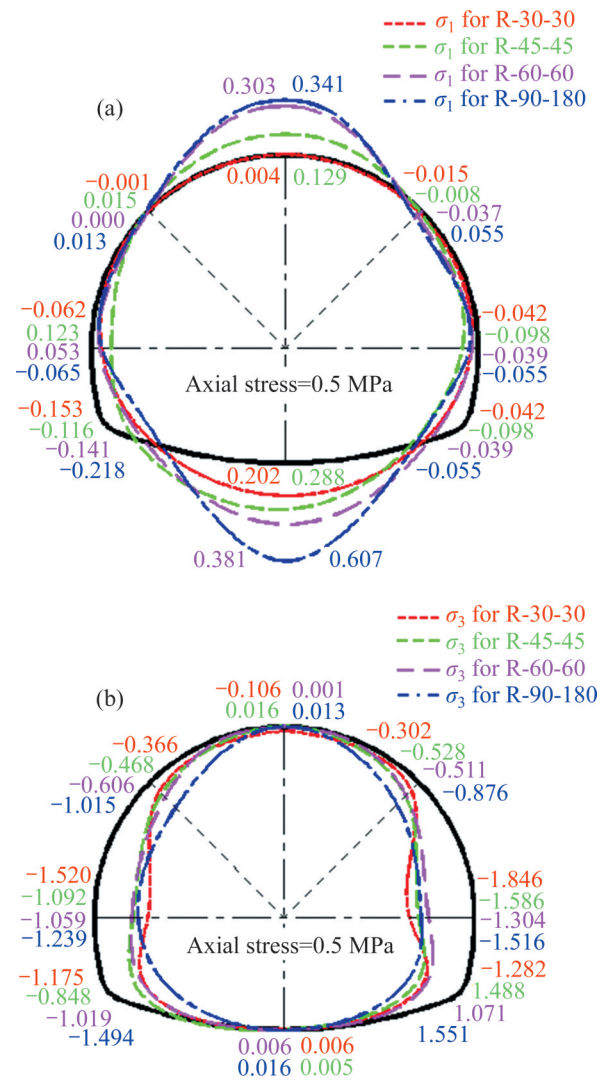


**Figure 8** Distribution of principal stress around four-arc-shaped tunnel (unit: MPa): (a) Maximum principal axial stress ( $\sigma_1$ ); (b) Minimum principal axial stress ( $\sigma_3$ )

stress at the vault and arch bottom of the two tunnels has a certain correlation with the fracture combination type. For the specimens with fracture combinations of  $30^\circ$ - $30^\circ$ , the tensile stress at the vault is approximately zero, but the tensile stress of the arch bottom is large. With an increase in the absolute value of fracture inclination angle ( $30^\circ \rightarrow 45^\circ \rightarrow 60^\circ$ ), the tensile stress at the vault and arch bottom of the two tunnels gradually increases. However, with a decrease in the absolute value of the preexisting fracture inclination angle, the compressive stress around the two tunnels near the hance (sidewall) increases. The compressive stress at the arch springing follows the same law. However, the change law of the compressive stress at the spandrel is the opposite. In addition, for the

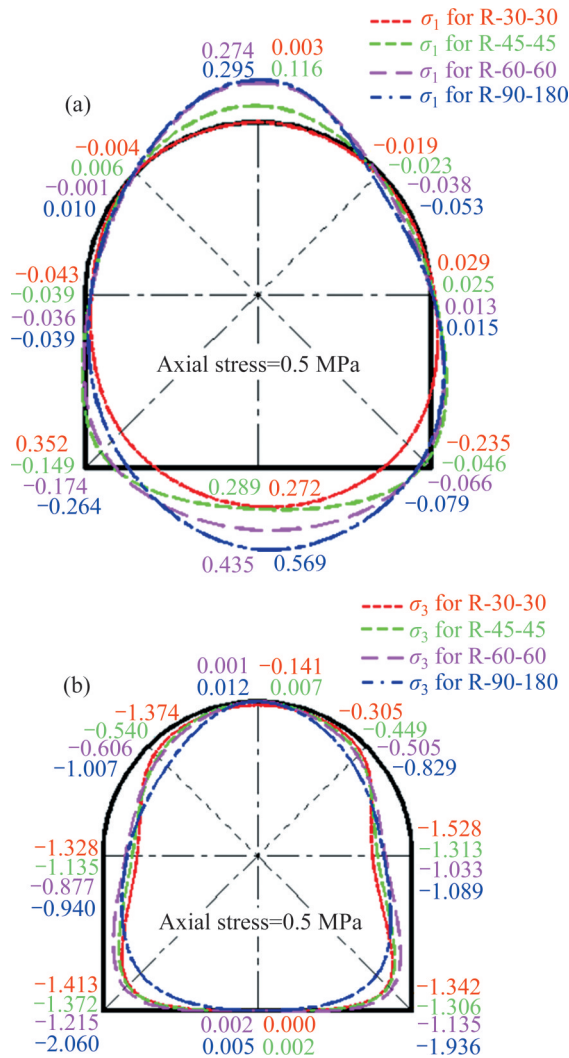


**Figure 9** Distribution of principal axial stress around inverted U-shaped tunnel (unit: MPa): (a) Maximum principal axial stress ( $\sigma_1$ ); (b) Minimum principal axial stress ( $\sigma_3$ )

fractured tunnel specimens with the same fracture combination type, near the vault and arch bottom, the maximum principal stress  $\sigma_1(U)$  in the inverted U-shaped tunnel was less than the maximum principal stress  $\sigma_1(R)$  in the four-arc-shaped tunnel. The absolute value of the minimum principal stress  $|\sigma_3(U)|$  in the inverted U-shaped tunnel was less than the absolute value of the minimum principal stress  $|\sigma_3(R)|$  in the four-arc-shaped tunnel near the hance (sidewall). And  $\sigma_1(R)$  is higher than  $\sigma_1(U)$  near the arch springing. Hence, the stress around the four-arc-shaped tunnel is relatively uniform, while the compressive stress of the inverted U-shaped tunnel is concentrated near the arch springing, which is prone to shear failure or

compression–shear failure.

To analyze the critical cracking stress around the tunnel, cracks initiated around the tunnel (S-T-CI) were evaluated, and the critical cracking stress characteristics of each model were presented. As shown in Figures 10 and 11, at the vault and arch bottom of the two tunnels, the tensile stress was proportional to the absolute value of the preexisting fracture inclination angle. In the specimens with a preexisting fracture combination of  $90^\circ$ – $180^\circ$ , the tensile stress near the vault and arch bottom was less than that of the specimens with a preexisting fracture combination of  $60^\circ$ – $60^\circ$ .  $|\sigma_1(R-60-60)| > |\sigma_1(R-90-180)| > |\sigma_1(R-45-45)| > |\sigma_1(R-30-30)|$ ,  $|\sigma_1(U-60-60)| > |\sigma_1(U-90-180)| > |\sigma_1(U-45-45)| > |\sigma_1(U-30-30)|$ .

There was no difference in the distribution of the compressive stress in the hance (sidewall)

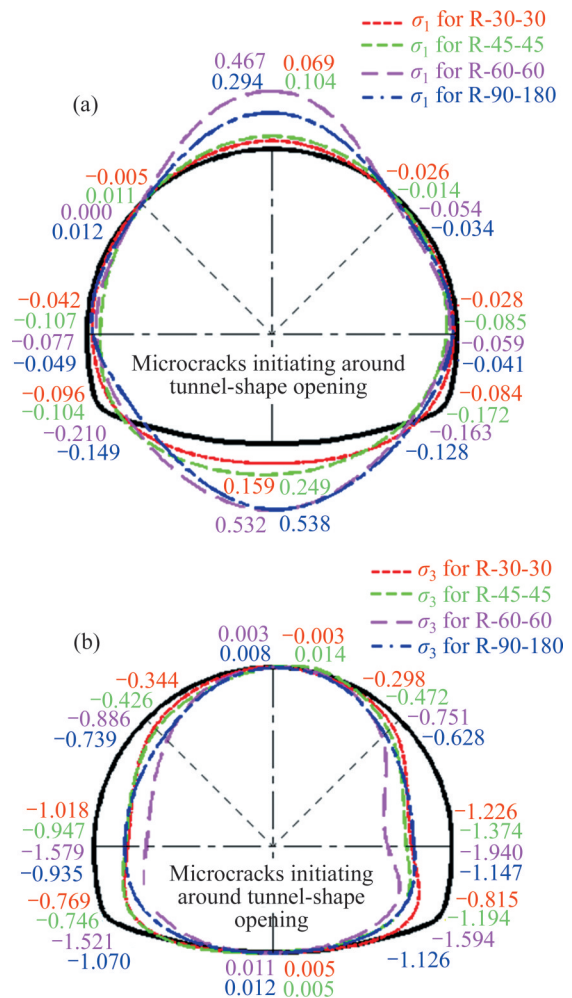


**Figure 10** Distribution of principal tensile stress around four-arc-shaped tunnel (unit: MPa): (a) Maximum principal tensile stress ( $\sigma_1$ ); (b) Minimum principal tensile stress ( $\sigma_3$ )

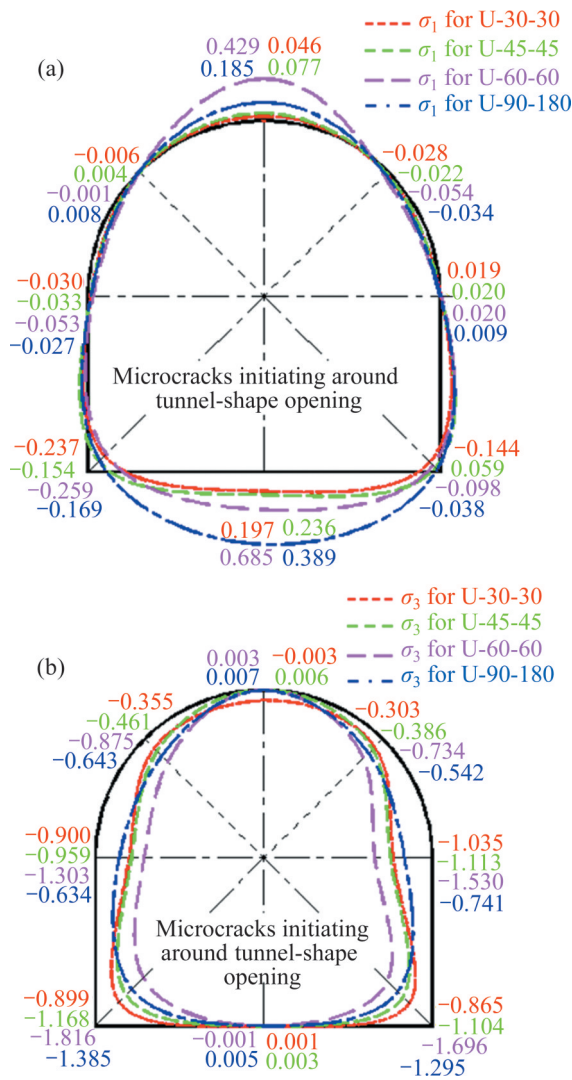


**Figure 11** Distribution of principal tensile stress around inverted U-shaped tunnel (unit: MPa): (a) Maximum principal tensile stress ( $\sigma_1$ ); (b) Minimum principal tensile stress ( $\sigma_3$ )

between the two tunnel types. Here,  $|\sigma_3|(\text{R-60-60}) > |\sigma_3|(\text{R-45-45}) > |\sigma_3|(\text{R-30-30}) > |\sigma_3|(\text{R-90-180})$ ,  $|\sigma_3|(\text{U-60-60}) > |\sigma_3|(\text{U-45-45}) > |\sigma_3|(\text{U-30-30}) > |\sigma_3|(\text{U-90-180})$ .

This indicates that when the fractures are almost vertical, the stress of the sidewall force of the four-arc-shaped tunnel is significantly affected. When the fractures are almost horizontal, the stress on the sidewall of the inverted U-shaped tunnel is significantly affected. This is mainly due to the relatively uniform stress around the four-arc-shaped (quasi-circular) tunnel and comparatively strong bearing capacity. However, under the action of axial stress, when the preexisting fractures are almost vertical, cracking is easily caused by the stress concentration at the arch springing of the inverted

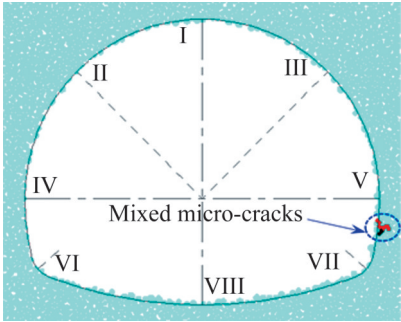
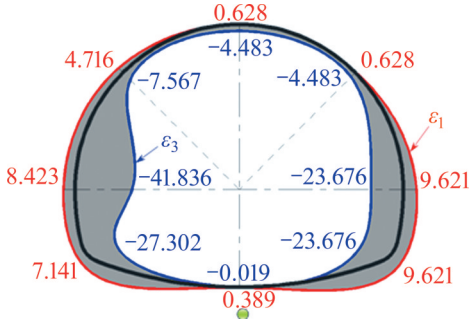
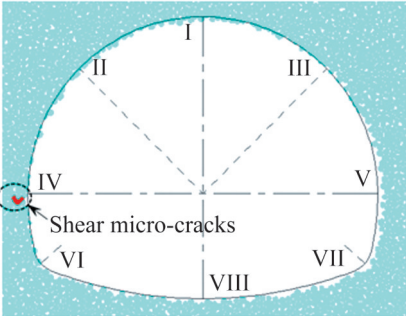
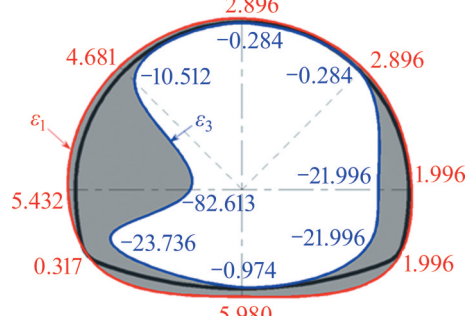
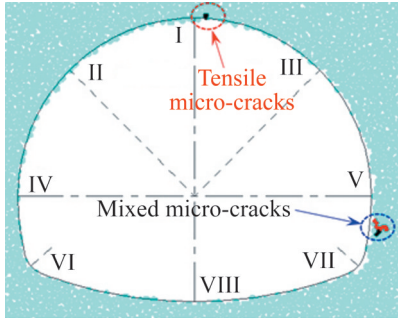
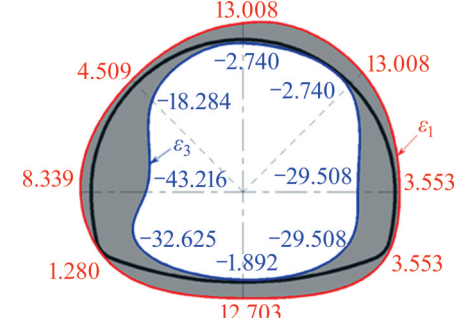
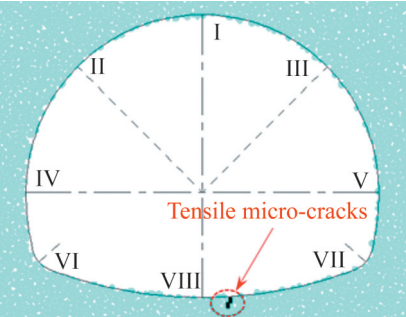
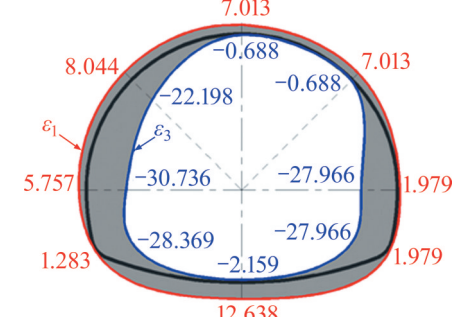
U-shaped tunnel. Therefore, the stress around the tunnel is less during failure.

### 4.3 Correlation analysis of crack initiation type and principal strain around tunnel

By monitoring the strain using numerical modeling, and on the basis of material mechanics formulae, the distribution characteristics of the maximum principal strain and the minimum principal strain around the tunnel were determined. Subsequently, the correlation between crack initiation and strain distribution was studied. It can be seen from Table 6 that the four-arc-shaped tunnel was prone to crack initiation at the vault, arch bottom, and hance. When the combination type of fracture inclination angle was 30°-30°, sidewall cracks first appeared near the right hance and were predominantly mixed micro-fractures. Here, the corresponding compressive and tensile strain ratio  $\left| \frac{\sigma_3}{\sigma_1} \right|$ , see Table 6, type of flaw 30°-30°) was

approximately 2.5, but the tensile strain was the largest. It can be seen that cracking in this type of tunnel was mainly caused by surface splitting failure. When the fracture inclination angle combination type was 45°-45°, shear cracks were the dominant type of cracks in the left hance. The corresponding compressive and tensile strain ratio was approximately 15.3, and the tensile strain was less than that at the arch bottom. When the fracture inclination angle combination type was 60°-60°, the mixed cracks were the dominant type of cracks in the left hance. The corresponding compressive and tensile strain ratios were approximately 8.4, and shear cracks were predominantly observed. Thus, for the four-arc-shaped tunnel model, the generation of shear micro-fractures was mainly determined by the compressive strain, and the ratio of the compressive strain to tensile strain was approximately 10. When the tensile strain around the surrounding rock reached a certain value, tensile micro-fractures occurred. In addition, in the four-arc-shaped tunnel, mixed micro-fractures (tensile micro-fractures and shear micro-fractures) could easily be observed near the hance. The types of macroscopic cracks are further determined by the relative magnitudes of the tensile and compressive strains.

**Table 6** Distribution of micro-crack and strain around four-arc-shaped tunnel (when the axial stress was equal to the crack initiation stress)

Type of flaws	Cracking around opening	Principal strain around opening/ $10^{-4}$
30°-30°		
45°-45°		
60°-60°		
90°-90°		

The correlation between the types of cracks initiated and the principal strain around the inverted U-shaped tunnel model was similar to that around the four-arc-shaped tunnel model. Cracks around the tunnel were mainly initiated in the vault, hence, and arch springing (Table 7). The occurrence of tensile micro-fractures was mainly determined by the

tensile strain value, and the generation of shear micro-fractures was directly determined by the compressive strain. Moreover, when compared with the four-arc-shaped tunnel, for the tunnel model with the same fracture combination type, when the cracks appeared around the inverted U-shaped tunnel, the sidewall compressive stress was smaller

**Table 7** Distribution of micro-crack and strain around inverted U-shaped tunnel (When the axial stress was equal to the crack initiation stress)

Type of flaws	Cracking around opening	Principal strain around opening /10 <sup>-4</sup>
30°-30°		
45°-45°		
60°-60°		
90°-90°		

than that of the former, while the vault tensile strain was larger than that of the former.

### 5 Conclusions

1) When combined with the evolution characteristics of cracks around the tunnel, the

larger the absolute value of the preexisting fracture inclination angle, the higher is the crushing degree of compression splitting near the hance (M-4 and M-5) and the larger the V-shaped failure zone. Moreover, cracks gradually develop around the opening and are mainly distributed in the vault (M-1), arch bottom (M-8), and hance (M-4 and

M-5). However, with an increase in the absolute value of the preexisting fracture inclination angle, the initiation sequence of cracks around the tunnel gradually shifts from the hance (M-4 and M-5) to the arch vault (M-1).

2) With a decrease in the absolute value of the preexisting fracture inclination angle ( $60^\circ \rightarrow 45^\circ \rightarrow 30^\circ$ ), the compressive stress concentration of the sidewall with preexisting fractures gradually increases. Concurrently, the tensile stress concentration near the vault and arch bottom reduces, and the compressive stress concentration near the hance reduces. Under the action of an external load, during the downward transmission of axial stress, a triangular tensile stress zone appears around the preexisting fracture sidewall in the horizontal direction, which causes a certain loss in the axial stress.

3) On the same axial stress level, the tensile stress at the vault and arch bottom has a certain correlation with the fracture combination type. Near the hance (sidewall), the compressive stress around the two tunnels increases with a decrease in the absolute value of the preexisting fracture inclination angle, and the same behavior is observed at the arch springing. However, the change law of the compressive stress at the spandrel is the opposite. In addition, for the fractured tunnel specimens with the same fracture combination type, the principal stress near the vault and arch bottom is  $\sigma_3(R) > \sigma_3(U)$ , and  $\sigma_1(R) > \sigma_1(U)$  near the hance (sidewall).

4) When the fractures are almost vertical, they have a significant influence on the stress of the sidewall force of the four-arc-shaped tunnel. When the fractures are almost horizontal, they have a significant influence on the stress of the sidewall of the inverted U-shaped tunnel. This is mainly due to the relatively uniform stress around the four-arc-shaped (quasi-circular) tunnel and its comparatively strong bearing capacity. However, under the action of axial stress, when the preexisting fractures are almost vertical, the stress concentration at the arch springing of the inverted U-shaped tunnel can easily cause cracking. Therefore, the stress around the tunnel is less during failure.

5) There is a significant relationship between the type of micro-fractures initiated around the

tunnel and the distribution of principal strain. When the maximum principal strain reaches its peak, it is accompanied by the generation of tensile micro-fractures. The generation of shear micro-fractures is mainly determined by the minimum principal strain. In addition, mixed micro-fractures (tensile micro-fractures and shear micro-fractures) can be easily observed near the hance of the four-arc-shaped tunnel. The types of macroscopic cracks are further determined by the relative magnitudes of the tensile and compressive strains.

## Contributors

FAN Xiang provided the concept and wrote the first draft of the manuscript. YANG Zhi-jun analyzed the measured data and edited the draft of manuscript. HONG Ming conducted the literature review and wrote the first draft of manuscript. YU Hao verified the data. XIE Yong-li provided support for the manuscript. All authors replied to reviewers' comments and revised the final version.

## Conflict of interest

FAN Xiang, YANG Zhi-jun, HONG Ming, YU Hao and XIE Yong-li declare that they have no conflict of interest.

## References

- [1] BOBET A. The initiation of secondary cracks in compression [J]. *Engineering Fracture Mechanics*, 2000, 66(2): 187–219. DOI: 10.1016/S0013-7944(00)00009-6.
- [2] GERMANOVICH L N, SALGANIK R L, DYSKIN A V, et al. Mechanisms of brittle fracture of rock with pre-existing cracks in compression [J]. *Pure and Applied Geophysics*, 1994, 143(1–3): 117–149. DOI: 10.1007/BF00874326.
- [3] LUO Yong, GONG Feng-qiang, LIU Dong-qiao, et al. Experimental simulation analysis of the process and failure characteristics of spalling in D-shaped tunnels under true-triaxial loading conditions [J]. *Tunnelling and Underground Space Technology*, 2019, 90: 42–61. DOI: 10.1016/j.tust.2019.04.020.
- [4] YU Jin, LIU Geng-yun, CAI Yan-yan, et al. Time-dependent deformation mechanism for swelling soft-rock tunnels in coal mines and its mathematical deduction [J]. *International Journal of Geomechanics*, 2020, 20(3): 04019186. DOI: 10.1061/(asce)gm.1943-5622.0001594.
- [5] BAUD P, REUSCHLÉ T, CHARLEZ P. An improved wing crack model for the deformation and failure of rock in compression [J]. *International Journal of Rock Mechanics and Mining Sciences & Geomechanics Abstracts*, 1996, 33(5): 539–542. DOI: 10.1016/0148-9062(96)00004-6.

- [6] GOLSHANI A, OKUI Y, ODA M, et al. A micromechanical model for brittle failure of rock and its relation to crack growth observed in triaxial compression tests of granite [J]. *Mechanics of Materials*, 2006, 38(4): 287–303. DOI: 10.1016/j.mechmat.2005.07.003.
- [7] QIAN Xi-kun, LIANG Zheng-zhao, LIAO Zhi-yi, et al. Numerical investigation of dynamic fracture in rock specimens containing a pre-existing surface flaw with different dip angles [J]. *Engineering Fracture Mechanics*, 2020, 223: 106675. DOI: 10.1016/j.engfracmech.2019.106675.
- [8] WONG L N Y, EINSTEIN H H. Crack coalescence in molded gypsum and Carrara marble: Part 2—Microscopic observations and interpretation [J]. *Rock Mechanics and Rock Engineering*, 2009, 42(3): 513–545. DOI: 10.1007/s00603-008-0003-3.
- [9] WONG L N Y, LI Huan-qiang. Numerical study on coalescence of two pre-existing coplanar flaws in rock [J]. *International Journal of Solids and Structures*, 2013, 50(22–23): 3685–3706. DOI: 10.1016/j.ijsolstr.2013.07.010.
- [10] YU Jin, YAO Wei, DUAN Kang, et al. Experimental study and discrete element method modeling of compression and permeability behaviors of weakly anisotropic sandstones [J]. *International Journal of Rock Mechanics and Mining Sciences*, 2020, 134: 104437. DOI: 10.1016/j.ijrmms.2020.104437.
- [11] CHEN Xin, LIAO Zhi-hong, PENG Xi. Cracking process of rock mass models under uniaxial compression [J]. *Journal of Central South University*, 2013, 20(6): 1661–1678. DOI: 10.1007/s11771-013-1660-2.
- [12] CHIU C C, WANG T T, WENG M C, et al. Modeling the anisotropic behavior of jointed rock mass using a modified smooth-joint model [J]. *International Journal of Rock Mechanics and Mining Sciences*, 2013, 62: 14–22. DOI: 10.1016/j.ijrmms.2013.03.011
- [13] FAN Xiang, KULATILAKE P H S W, CHEN Xin, et al. Crack initiation stress and strain of jointed rock containing multi-cracks under uniaxial compressive loading: A particle flow code approach [J]. *Journal of Central South University*, 2015, 22(2): 638–645. DOI: 10.1007/s11771-015-2565-z.
- [14] FAN Xiang, KULATILAKE P H S W, CHEN Xin. Mechanical behavior of rock-like jointed blocks with multi-non-persistent joints under uniaxial loading: A particle mechanics approach [J]. *Engineering Geology*, 2015, 190: 17–32. DOI: 10.1016/j.enggeo.2015.02.008.
- [15] SATO A, HIRAKAWA Y, SUGAWARA K. Mixed mode crack propagation of homogenized cracks by the two-dimensional DDM analysis [J]. *Construction and Building Materials*, 2001, 15(5–6): 247–261. DOI: 10.1016/S0950-0618(00)00074-X.
- [16] WEI Ming-dong, DAI Feng, ZHOU Jia-wen, et al. A further improved maximum tangential stress criterion for assessing mode I fracture of rocks considering non-singular stress terms of the williams expansion [J]. *Rock Mechanics and Rock Engineering*, 2018, 51(11): 3471–3488. DOI: 10.1007/s00603-018-1524-z.
- [17] YAN Ze-lin, DAI Feng, LIU Yi, et al. Experimental and numerical investigation on the mechanical properties and progressive failure mechanism of intermittent multi-jointed rock models under uniaxial compression [J]. *Arabian Journal of Geosciences*, 2019, 12(22): 1–24. DOI: 10.1007/s12517-019-4737-x.
- [18] CHANG Xu, DENG Yan, LI Zhen-hua, et al. Crack propagation from a filled flaw in rocks considering the infill influences [J]. *Journal of Applied Geophysics*, 2018, 152: 137–149. DOI: 10.1016/j.jappgeo.2018.03.018.
- [19] ZHUANG Xiao-ying, CHUN Jun-wei, ZHU He-hua. A comparative study on unfilled and filled crack propagation for rock-like brittle material [J]. *Theoretical and Applied Fracture Mechanics*, 2014, 72: 110–120. DOI: 10.1016/j.tafmec.2014.04.004.
- [20] CARTER B J, LAJTAI E Z, YUAN Yan-guang. Tensile fracture from circular cavities loaded in compression [J]. *International Journal of Fracture*, 1992, 57(3): 221–236. DOI: 10.1007/BF00035074.
- [21] CARTER B J. Size and stress gradient effects on fracture around cavities [J]. *Rock Mechanics and Rock Engineering*, 1992, 25(3): 167–186. DOI: 10.1007/BF01019710.
- [22] GONG Feng-qiang, LUO Yong, LI Xi-bing, et al. Experimental simulation investigation on rockburst induced by spalling failure in deep circular tunnels [J]. *Tunnelling and Underground Space Technology*, 2018, 81: 413–427. DOI: 10.1016/j.tust.2018.07.035.
- [23] YANG Xu-xu, JING Hong-wen, CHEN Kun-fu, et al. Failure behavior around a circular opening in a rock mass with non-persistent joints: A parallel-bond stress corrosion approach [J]. *Journal of Central South University*, 2017, 24(10): 2406–2420. DOI: 10.1007/s11771-017-3652-0.
- [24] ZHOU X P, BAO X R, YU M H, et al. Triaxial stress state of cylindrical openings for rocks modeled by elastoplasticity and strength criterion [J]. *Theoretical and Applied Fracture Mechanics*, 2010, 53(1): 65–73. DOI: 10.1016/j.tafmec.2009.12.006.
- [25] ZHU W C, BRUHNS O T. Simulating excavation damaged zone around a circular opening under hydromechanical conditions [J]. *International Journal of Rock Mechanics and Mining Sciences*, 2008, 45(5): 815–830. DOI: 10.1016/j.ijrmms.2007.09.007.
- [26] GAY N C. Fracture growth around openings in thick-walled cylinders of rock subjected to hydrostatic compression [J]. *International Journal of Rock Mechanics and Mining Sciences & Geomechanics Abstracts*, 1973, 10(3): 209–233. DOI: 10.1016/0148-9062(73)90032-6.
- [27] CAI M, KAISER P K, TASAKA Y, et al. Determination of residual strength parameters of jointed rock masses using the GSI system [J]. *International Journal of Rock Mechanics and Mining Sciences*, 2007, 44(2): 247–265. DOI: 10.1016/j.ijrmms.2006.07.005.
- [28] ZHONG Zhi-bin, DENG Rong-gui, LV Lei, et al. Fracture mechanism of naturally cracked rock around an inverted U-shaped opening in a biaxial compression test [J]. *International Journal of Rock Mechanics and Mining Sciences*, 2018, 103: 242–253. DOI: 10.1016/j.ijrmms.2018.01.047.
- [29] YANG Sheng-qi, TIAN Wen-ling, HUANG Yan-hua, et al. Experimental and discrete element modeling on cracking behavior of sandstone containing a single oval flaw under uniaxial compression [J]. *Engineering Fracture Mechanics*,



- 2018, 194: 154 – 174. DOI: 10.1016/j.engfracmech.2018.03.003.
- [30] ZHU Wei-shen, LI Yong, LI Shu-cai, et al. Quasi-three-dimensional physical model tests on a cavern complex under high in situ stresses [J]. *International Journal of Rock Mechanics and Mining Sciences*, 2011, 48(2): 199 – 209. DOI: 10.1016/j.ijrmms.2010.11.008.
- [31] WANG Wen-cai, WANG Zheng, ZHANG An, et al. Simulation study on propagation law of double-hole permeability improvement cracks with joints [J]. *Safety in Coal Mines*, 2019, 50(9): 21 – 24. DOI: 10.13347/j.cnki.mkaq.2019.09.007. (in Chinese)
- [32] DU Ming-rui, JING Hong-wen, SU Hai-jian, et al. Strength and failure characteristics of sandstone containing two circular holes filled with two types of inclusions under uniaxial compression [J]. *Journal of Central South University*, 2017, 24(11): 2487–2495. DOI: 10.1007/s11771-017-3661-z.
- [33] CAO Ri-hong, CAO Ping, LIN Hang, et al. Mechanical behavior of an opening in a jointed rock-like specimen under uniaxial loading: Experimental studies and particle mechanics approach [J]. *Archives of Civil and Mechanical Engineering*, 2018, 18(1): 198 – 214. DOI: 10.1016/j.acme.2017.06.010.
- [34] CHEN Hao, FAN Xiang, LAI Hong-peng, et al. Experimental and numerical study of granite blocks containing two side flaws and a tunnel-shaped opening [J]. *Theoretical and Applied Fracture Mechanics*, 2019, 104: 102394. DOI: 10.1016/j.tafmec.2019.102394.
- [35] FAN Xiang, CHEN Rui, LIN Hang, et al. Cracking and failure in rock specimen containing combined flaw and hole under uniaxial compression [J]. *Advances in Civil Engineering*, 2018, 2018: 9818250. DOI: 10.1155/2018/9818250.
- [36] FAN Xiang, LI Kai-hui, LAI Hong-peng, et al. Internal stress distribution and cracking around flaws and openings of rock block under uniaxial compression: A particle mechanics approach [J]. *Computers and Geotechnics*, 2018, 102: 28–38. DOI: 10.1016/j.compgeo.2018.06.002.
- [37] WANG Yi-xian, ZHANG Hui, LIN Hang, et al. Fracture behaviour of central-flawed rock plate under uniaxial compression [J]. *Theoretical and Applied Fracture Mechanics*, 2020, 106: 102503. DOI: 10.1016/j.tafmec.2020.102503.
- [38] FAN Xiang, JIANG Xu-dong, LIU Yi-xin, et al. Local stress distribution and evolution surrounding flaw and opening within rock block under uniaxial compression [J]. *Theoretical and Applied Fracture Mechanics*, 2021, 112: 102914. DOI: 10.1016/j.tafmec.2021.102914.
- [39] FAN Xiang, YANG Zhi-jun, LI Kai-hui. Effects of the lining structure on mechanical and fracturing behaviors of four-arc shaped tunnels in a jointed rock mass under uniaxial compression [J]. *Theoretical and Applied Fracture Mechanics*, 2021, 112: 102887. DOI: 10.1016/j.tafmec.2020.102887.
- [40] ZHANG Chun-yang, PU Cheng-zhi, CAO Ri-hong, et al. The stability and roof-support optimization of roadways passing through unfavorable geological bodies using advanced detection and monitoring methods, among others, in the Sanmenxia Bauxite Mine in China’s Henan Province [J]. *Bulletin of Engineering Geology and the Environment*, 2019, 78(7): 5087–5099. DOI: 10.1007/s10064-018-01439-1.
- (Edited by YANG Hua)

## 中文导读

### 裂隙化类岩材料中两种不同形状开孔周围的应力分布和破坏机理

**摘要：**岩体结构的复杂性会导致地下工程在施工过程中的高度不确定性和风险。本研究采用类岩材料室内试验和二维颗粒流数值模拟相结合的方式，分别研究了四心圆形隧道和马蹄形隧道周围的主应力和主应变分布。数值结果表明，既有的裂隙倾角组合直接影响隧道周围的主应力、主应变分布和破坏特征。预裂隙的倾角绝对值越大，两类隧洞均在拱腰(M-4和M-5)附近的挤压劈裂破碎程度逐渐加剧，“V”形破坏区也越大。随着预裂隙倾角绝对值的减小(60°→45°→30°)，预裂隙的侧壁压应力集中程度逐渐增加。四心圆形隧道和马蹄形隧道周围产生的裂缝类型不同。当裂隙近于垂直时，对四心圆形隧洞侧壁受力影响较大；而当裂隙近于水平时，对马蹄形隧洞边墙受力影响较大。以上发现，为隧道支护结构的局部加固设计提供了理论支持。

**关键词：**隧洞；裂隙化类岩材料；二维颗粒流；裂纹起裂；应力分布